Symmetry energy in nuclear density functional theory

Nazarewicz, W.; Reinhard, P. - G.; Satula, W.; Vretenar, Dario

Source / Izvornik: **European Physical Journal A: Hadrons and Nuclei, 2014, 50**

Journal article, Published version
Rad u časopisu, Objavljena verzija rada (izdavačev PDF)

https://doi.org/10.1140/epja/i2014-14020-3

Eur. Phys. J. A (2014) **50**: 20
DOI 10.1140/epja/i2014-14020-3

THE EUROPEAN PHYSICAL JOURNAL A

Regular Article – Theoretical Physics

Symmetry energy in nuclear density functional theory[⋆]

W. Nazarewicz[1,2,3,a], P.-G. Reinhard[4], W. Satuła[3], and D. Vretenar[5]

[1] Department of Physics and Astronomy, University of Tennessee Knoxville, Tennessee 37996, USA
[2] Oak Ridge National Laboratory, P.O. Box 2008, Oak Ridge, Tennessee 37831, USA
[3] Faculty of Physics, University of Warsaw, ul. Hoża 69, 00-681 Warsaw, Poland
[4] Institut für Theoretische Physik, Staudtstr. 7 D-90158 Universität Erlangen/Nürnberg, Erlangen, Germany
[5] Physics Department, Faculty of Science, University of Zagreb, Zagreb, Croatia

Received: 22 July 2013 / Revised: 22 August 2013

Communicated by A. Ramos

Abstract. The nuclear symmetry energy represents a response to the neutron-proton asymmetry. In this paper we discuss various aspects of symmetry energy in the framework of nuclear density functional theory, considering both non-relativistic and relativistic self-consistent mean-field realizations side by side. Key observables pertaining to bulk nucleonic matter and finite nuclei are reviewed. Constraints on the symmetry energy and correlations between observables and symmetry energy parameters, using statistical covariance analysis, are investigated. Perspectives for future work are outlined in the context of ongoing experimental efforts.

1 Introduction

Density Functional Theory (DFT) is a universal approach used to describe properties of complex, strongly correlated many-body systems. Originally developed in the context of many-electron systems in condensed matter physics and quantum chemistry [1,2] (also known under the name of Kohn-Sham DFT), it is also a tool of choice in microscopic studies of complex heavy nuclei. The basic implementation of this framework is in terms of self-consistent mean-field (SCMF) models [3–5].

Extending the DFT to atomic nuclei, the nuclear DFT, is not straightforward as nuclei are self-bound, small, superfluid aggregations of two kinds of fermions, governed by strong surface effects. Their smallness leads to appreciable quantal fluctuations (finite-size effects) which are difficult to incorporate into the energy density functional (EDF). The lack of external binding potential implies that the nuclear DFT must be necessarily formulated in terms of intrinsic normal and anomalous (pairing) densities [6]. A density matrix expansion of the effective interaction suggests that, in addition to the standard local nucleon density, superior EDFs should also include more involved nucleon aggregates such as the kinetic-energy density and spin-orbit density [3–5]

The commonly used single-reference SCMF methods include the local (Skyrme), non-local (Gogny) and covariant (relativistic) approaches [5,7,8]. All these approaches are thought to be different realizations of an underlying effective field theory [9] with the ultraviolet physics hidden in free parameters adjusted to observations. For that reason, predictions for low-energy (infrared) physics should be fairly independent of the particular variant used in calculations [10–13]. The underlying EDFs are constructed in a phenomenological way, with coupling constants optimized to selected nuclear data and expected properties of homogeneous nuclear matter.

In practice, nuclear EDFs differ in their functional form and are subject to different optimization strategies causing that their predictions vary even within a single family of EDFs. In particular, large uncertainties remain in the isovector channel, which is poorly constrained by experiment. A key quantity characterizing the interaction in the isovector channel is the nuclear symmetry energy (NSE) describing the static response of the nucleus to the neutron-proton asymmetry.

As discussed in this *Topical Issue*, the NSE influences a broad spectrum of phenomena, ranging from subtle isospin mixing effects in $N \sim Z$ nuclei to particle stability of neutron-rich nuclei, to nuclear collective modes, and to radii and masses of neutron stars. Various nuclear observables are sensitive probes of NSE, and numerous phenomenological indicators can be constructed to probe its various aspects.

It is the aim of this contribution to analyze the relations between NSE and measurable observables in finite nuclei. The most promising observables for isovector properties that have stimulated vigorous experimental and

---

[⋆] Contribution to the Topical Issue "Nuclear Symmetry Energy" edited by Bao-An Li, Àngels Ramos, Giuseppe Verde, Isaac Vidaña.

[a] e-mail: `witek@utk.edu`

theoretical activity include neutron radii, neutron skins, dipole polarizability, and neutron star radii. The ongoing efforts are focused on better constraining the uncertainties concerning the equation of state (EOS) of the symmetric and asymmetric nucleonic matter (NM) and, in particular, the symmetry energy and its density dependence. Parameters that characterize the NSE are not entirely independent. They are affected by key nuclear observables in different ways. Thus it is the *sine qua non* of a further progress in this area to understand the correlation pattern between NSE parameters and finite-nuclei observables, and to provide uncertainty quantification on theoretical predictions using the powerful methods of statistical analysis [14].

A second aim is to understand the dependences from a formal perspective and to explore the impact of configuration mixing. Within the independent particle picture the isovector response can be described in terms of a charge-dependent symmetry potential that shifts the neutron well with respect to the proton average potential. The effect can be estimated quantitatively within the Fermi-gas model (FGM) augmented by a schematic isospin-isospin interaction [15],

$$V_{TT} = \frac{1}{2}\kappa \hat{\boldsymbol{T}} \cdot \hat{\boldsymbol{T}}. \tag{1}$$

In the Hartree approximation this model gives rise to a quadratic dependence of the NSE on the neutron excess $I = (N - Z)/A$,

$$E_{\mathrm{sym}}/A = a_{\mathrm{sym}} I^2 = (a_{\mathrm{sym,kin}} + a_{\mathrm{sym,int}}) I^2, \tag{2}$$

as $T = |T_z| = |N - Z|/2$ in the ground states of almost all nuclei. The FGM, in spite of its simplicity, has played an important role in our understanding of the NSE. In particular, it separates the NSE strength into kinetic and interaction (potential) contributions, and predicts a near-equality $a_{\mathrm{sym,kin}} \approx a_{\mathrm{sym,int}}$ of these contributions. It also provides an estimate $a_{\mathrm{sym}} \approx 25\,\mathrm{MeV}$ for the NSE coefficient (see ref. [16] for a recent discussion).

Furthermore, we note that the SCMF approach can lead to spontaneous breaking of symmetries. This apparent drawback can be turned into an advantage, as the symmetry breaking mechanism allows to incorporate many inter-nucleon correlations within a single product state or, alternatively, within a single-reference DFT sacrificing good quantum numbers; broken symmetries have to be restored *a posteriori*. We will address this topic using the example of isospin mixing which naturally has an impact on isovector properties.

This survey is organized as follows. Section 2 outlines the SCMF approaches and details various theoretical ingredients of the models employed in this work. Observables pertaining to bulk NM and finite nuclei that are essential for NSE are discussed in sect. 3. Constraints on NSE and correlations between observables and NSE parameters, using the statistical covariance technique, are presented in sect. 4. Section 5 summarizes the current status of NSE parameters. The planned extensions of the current DFT work are laid out in sect. 6. Finally, sect. 7 contains the conclusions of this survey.

2 Nuclear DFT

The nuclear EDF constitutes a crucial ingredient for a set of DFT-based theoretical tools that enable an accurate description of ground-state properties, collective excitations, and large-amplitude dynamics over the entire chart of nuclides, from relatively light systems to superheavy nuclei, and from the valley of β-stability to the nucleon drip-lines. In general EDFs are not directly related to any specific microscopic inter-nucleon interaction, but rather represent universal functionals of nucleon densities and currents. With a small set of global parameters adjusted to empirical properties of nucleonic matter and to selected data on finite nuclei [17,18], models based on EDFs enable a consistent description of a variety of nuclear structure phenomena.

The unknown exact and universal nuclear EDF is approximated by simple, mostly analytical, functionals built from powers and gradients of nucleonic densities and currents, representing distributions of matter, spins, momentum and kinetic energy. When pairing correlations are included, they are represented by pair (anomalous) densities. In the field of nuclear structure this method is analogous to Kohn-Sham DFT. SCMF models *effectively* map the nuclear many-body problem onto a one-body problem using auxilliary Kohn-Sham single-particle orbitals. By including many-body correlations in EDF, the Kohn-Sham method in principle goes beyond the Hartree-Fock (HF) or Hartree-Fock-Bogolyubov (HFB) approximations and, in addition, it has the advantage of using *local* potentials. A broad range of nuclear properties have been very successfully described using SCMF models based on Skyrme EDFs, relativistic EDFs, and the Gogny interaction [5,7,8,19–22]. (Note that the Gogny model is not strictly local as the other EDFs.) In the remainder of this section we briefly outline the Skyrme-Hartree-Fock (SHF) method and the relativistic mean-field (RMF) approach. As both methods are widely used and extensively described in the literature, we keep the presentation short and concentrate on a side-by-side comparison of the models.

The basis of any mean-field approach is a set of single-nucleon canonical (Kohn-Sham) orbitals $\psi_\alpha(\mathbf{r})$, with occupations amplitudes v_α. The ψ_α denote Dirac four-spinor wave functions in the RMF framework, and two-component-spinor wave functions in the SHF which is a classical mean-field model. The canonical occupation amplitudes v_α are determined by the pairing interaction. The starting point of a particular model is an EDF expressed in terms of ψ_α, v_α and the local densities derived therefrom. The energy functional for the SHF method reads

$$E = \int \mathrm{d}^3 r \; (\mathcal{E}_{\mathrm{kin}} + \mathcal{E}_{\mathrm{pot}}) + E_{\mathrm{Coul}} + E_{\mathrm{pair}} + E_{\mathrm{cm}}, \tag{3}$$

$$\mathcal{E}_{\mathrm{kin}} = \frac{\hbar^2}{2m_{\mathrm{p}}}\tau_{\mathrm{p}} + \frac{\hbar^2}{2m_{\mathrm{n}}}\tau_{\mathrm{n}}$$

$$E_{\mathrm{cm}} = -\frac{1}{2mA}\langle (\hat{P}_{\mathrm{cm}})^2 \rangle.$$

The kinetic energy $\mathcal{E}_{\mathrm{kin}}$ is expressed in terms of single-nucleon wave functions. The Skyrme functional is

Table 1. Upper: The basic isoscalar ($T = 0$) and isovector ($T = 1$) local densities of SHF (left) and RMF (right). Lower: The potential-energy densities in the three considered SCMF models. Model parameters (third row) defining the coupling constants are indicated by lowercase latin letters. For further explanation see text.

Densities			
SHF		RMF	
$T=0$	$T=1$	$T=0$	$T=1$
$\rho_0(\mathbf{r}) = \sum_\alpha v_\alpha^2\, \psi_\alpha^\dagger \psi_\alpha$	$\rho_1(\mathbf{r}) = \sum_\alpha v_\alpha^2\, \psi_\alpha^\dagger \hat{\tau}_3 \psi_\alpha$	$\rho_0(\mathbf{r}) = \sum_\alpha v_\alpha^2\, \psi_\alpha^\dagger \psi_\alpha$	$\rho_1(\mathbf{r}) = \sum_\alpha v_\alpha^2\, \psi_\alpha^\dagger \hat{\tau}_3 \psi_\alpha$
$\tau_0(\mathbf{r}) = \sum_\alpha v_\alpha^2\, \boldsymbol{\nabla}\psi_\alpha^\dagger \boldsymbol{\nabla}\psi_\alpha$	$\tau_1(\mathbf{r}) = \sum_\alpha v_\alpha^2\, \boldsymbol{\nabla}\psi_\alpha^\dagger \hat{\tau}_3 \boldsymbol{\nabla}\psi_\alpha$	$\rho_\mathrm{S}(\mathbf{r}) = \sum_\alpha v_\alpha^2\, \psi_\alpha^\dagger \hat{\gamma}_0 \psi_\alpha$	
$\mathbf{J}_0(\mathbf{r}) = -\mathrm{i} \sum_\alpha v_\alpha^2\, \psi_\alpha^\dagger \boldsymbol{\nabla} \times \hat{\boldsymbol{\sigma}} \psi_\alpha$	$\mathbf{J}_1(\mathbf{r}) = -\mathrm{i} \sum_\alpha v_\alpha^2\, \psi_\alpha^\dagger \hat{\tau}_3 \boldsymbol{\nabla} \times \hat{\boldsymbol{\sigma}} \psi_\alpha$		

	Potential-energy density					
	SHF		RMF-PC		RMF-ME	
	$T=0$	$T=1$	$T=0$	$T=1$	$T=0$	$T=1$
$\rho\rho$	$C_0^\rho \rho_0^2$	$C_1^\rho \rho_1^2$	$G_\omega \rho_0^2$	$G_\rho \rho_1^2$	$G_\omega \rho_0 \frac{1}{-\Delta + m_\omega^2} \rho_0$	$G_\rho \rho_1 \frac{1}{-\Delta + m_\rho^2} \rho_1$
mass	$C_0^\tau \rho_0 \tau_0$	$C_1^\tau \rho_1 \tau_1$	$G_\sigma \rho_\mathrm{S}^2$		$G_\sigma \rho_\mathrm{S} \frac{1}{-\Delta + m_\sigma^2} \rho_\mathrm{S}$	
$\boldsymbol{\ell} \cdot \boldsymbol{s}$	$C_0^{\boldsymbol{\nabla}\mathbf{J}} \rho_0 \boldsymbol{\nabla} \cdot \mathbf{J}_0$	$C_1^{\boldsymbol{\nabla}\mathbf{J}} \rho_1 \boldsymbol{\nabla} \cdot \mathbf{J}_1$	“		“	
gradient	$C_0^{\Delta\rho} (\boldsymbol{\nabla}\rho_0)^2$	$C_1^{\Delta\rho} (\boldsymbol{\nabla}\rho_1)^2$	$f_\mathrm{S} (\boldsymbol{\nabla}\rho_\mathrm{S})^2$			
dens. dep.	$C_0^\rho = c_0^\rho + d_0^\rho \rho_0^a$ $C_T^\tau = c_T^\tau\ ,\ C_T^{\Delta\rho} = c_T^{\Delta\rho}\ ,\ C_T^{\boldsymbol{\nabla}\mathbf{J}} = c_T^{\boldsymbol{\nabla}\mathbf{J}}$	$C_1^\rho = c_1^\rho + d_1^\rho \rho_0^a$	$G_i = a_i + (b_i + c_i x) e^{-d_i x}$ $i \in \{\sigma, \omega, \rho\},\ x = \frac{\rho_0}{\rho_\mathrm{sat}}$		$G_i = a_i \frac{1 + b_i (x + d_i)^2}{1 + c_i (x + d_i)^2}$ $i \in \{\sigma, \omega\},\ x = \frac{\rho_0}{\rho_\mathrm{sat}}$	$G_\rho = g_\rho e^{-a_\rho (x-1)}$

contained in the interaction part with the potential-energy density $\mathcal{E}_\mathrm{pot}$. The Coulomb energy E_Coul consists of the direct Coulomb term, and the Coulomb exchange that is usually taken into account at the level of the Slater approximation. In most applications the center-of-mass correction E_cm is applied *a posteriori* because its variation would considerably complicate the mean-field equations. The pairing functional E_pair will be detailed later. The RMF approach is usually formulated in terms of a Lagrangian,

$$L = \int \mathrm{d}^3 r\ (\mathcal{L}_\mathrm{kin} - \mathcal{E}_\mathrm{pot}) - E_\mathrm{Coul} - E_\mathrm{pair} - E_\mathrm{cm}, \quad (4)$$

$$\mathcal{L}_{kin} = \sum_\alpha v_\alpha^2 \psi_\alpha^\dagger \hat{\gamma}_0 (i\hat{\boldsymbol{\gamma}} \cdot \boldsymbol{\partial} - m) \psi_\alpha, \quad (5)$$

where $\hat{\gamma}$ is the Dirac matrix. Again, the kinetic part is expressed explicitly in terms of Dirac spinor wave functions, whereas interaction terms are included in the potential energy density $\mathcal{E}_\mathrm{pot}$. Further contributions from Coulomb, pairing and center-of-mass motion are treated similarly as in the SHF approach.

The basic building blocks of an EDF are local densities and currents built from single-nucleon wave functions [5, 23]. These are summarized in the upper part of table 1. All densities appear in two flavors [24,25]: isoscalar ($T = 0$), or total density (sum of proton and neutron densities), and isovector ($T = 1$) density (difference between neutron and proton densities). Both can be conveniently expressed using the isospin operator $\hat{\tau}_3$. The basic ingredients of an EDF are the local densities ρ_0 and ρ_1. In RMF these can be associated with the zero-component of the four-vector current, where ρ_0 is often called the vector density and ρ_1 the isovector-vector density. RMF uses one more ingredient, the isoscalar-scalar density denoted here as ρ_S. SHF instead employs the kinetic-energy densities $\tau_{0/1}$ and the spin-orbit densities $\mathbf{J}_{0/1}$. One can show that τ_0 and $\mathbf{J}_0$ emerge in the non-relativistic limit of ρ_S [26]. The principal difference between SHF and RMF is that the quantities τ_0 and $\mathbf{J}_0$ are independent in SHF, whereas they are tightly related through ρ_S in RMF. Moreover, the RMF does not invoke an isovector counterpart of ρ_S thus being more restricted in the isovector channel.

The lower part of table 1 displays the main components of the potential-energy density. The underlying is to take all bi-linear isoscalar combinations of the local densities and to associate a coupling constant with each term [25]. The SHF confines the combinations to have at most second order of derivatives (the term $\mathbf{J}^2$ is also dropped). In the RMF approach one keeps only terms that form a Lorentz scalar. Moreover, two bi-linear realizations of RMF will be considered. First there is the straightforward point-coupling (RMF-PC) realization that corresponds to contact interactions between nucleons and, second, the meson-exchange folding (RMF-ME). The folding is motivated by the traditional route to RMF as a model of nucleons coupled to classical meson fields. Of course, at energies characteristic for nuclear binding meson exchange represents just a convenient representation of the effective nuclear interaction. In practice RMF-PC and RMF-ME present equivalent realizations of the relativistic SCMF, differing in the range of effective interactions (zero range *vs.* finite range) and the choice of density dependence for the couplings. In practical applications one restricts the density dependence of coupling (vertex) functions to keep the number of free parameters to a minimum. In SHF, only the leading terms $\propto \rho_0^2$ and ρ_1^2 are given a (simple) density dependence as shown in table 1. In RMF-PC and RMF-ME, each term has some density dependence, but not all of these parameters are actually used. In RMF-PC, in particular, the parameters c_1 and a_1 (isovector channel) and $c_{\rm v}$ (isoscalar vector channel) are set to zero [27]. In RMF-ME, the parameters are correlated by additional boundary conditions on G_i [28,29]. In total, there are 11 adjustable parameters for SHF, 10 for RMF-PC, and 8 for RMF-ME. From a formal perspective, SHF and RMF-PC are rather similar, differing mainly in the relativistic kinematics, while RMF-ME includes a significantly different density dependence of the couplings, in addition to the finite range. These three models thus allow to display separately effects of kinematics, density dependence, and range of the effective nuclear interaction.

As far as particle-particle interaction is concerned, in the SHF we use the pairing functional derived from a density-dependent zero-range force,

$$E_{\rm pair} = \frac{1}{4} \sum_{q\in\{p,n\}} v_{0,q} \int {\rm d}^3 r \tilde{\rho}_q^2 \left[1 - \frac{\rho(\mathbf{r})}{\rho_{\rm pair}}\right], \tag{6a}$$

$$\tilde{\rho}_q(\mathbf{r}) = \sum_{\alpha\in q} u_\alpha v_\alpha \left|\psi_\alpha(\mathbf{r})\right|^2, \tag{6b}$$

where q runs over protons and neutrons. It involves the pair-density $\tilde{\rho}_q$ and is usually augmented by some density dependence. We consider here $v_{0,p}$, $v_{0,n}$, and $\rho_{\rm pair}$ as free parameters of the pairing functional in SHF. Note that we do not recouple to isoscalar and isovector terms because pairing is considered independently for protons and neutrons. Actually, the zero-range pairing force works only together with a limited phase space for pairing. We use here a soft cut-off in the space of single-nucleon energies [30] according to ref. [31].

In RMF calculations we use the recently developed separable pairing force [32,33]. It is separable in momentum space, and is completely determined by two parameters that are adjusted to reproduce in symmetric nuclear matter the pairing gap of the Gogny force. We have verified that both pairing prescriptions yield comparable results for the pairing gaps.

3 Observables

In this section, we discuss observables pertaining to nuclear matter (NM) and finite nuclei that are essential for discussion of NSE. Those observables can be roughly divided [14] into good isovector indicators that correlate very well with NSE (such as weak-charge form factor, neutron skins, dipole polarizability, slope of the symmetry energy, and neutron pressure) and poor isovector indicators (such as nuclear and neutron matter binding energy, giant resonance energies, isoscalar and isovector effective mass, incompressibility, and saturation density).

Table 2. Definitions of NMP used in this work. All derivatives are to be taken at the equilibrium point corresponding to the saturation density $\rho_{\rm eq}$.

Incompressibility:	K_∞	$=$	$9\,\rho_0^2 \frac{{\rm d}^2}{{\rm d}\rho_0^2} \frac{E}{A}\vert_{\rm eq}$
Symmetry energy:	$a_{\rm sym}$	$=$	$\frac{1}{2}\rho_0^2 \frac{{\rm d}^2}{{\rm d}\rho_1^2} \frac{E}{A}\vert_{\rm eq}$
Slope of $a_{\rm sym}$:	L	$=$	$3\rho_0 \frac{{\rm d}a_{\rm sym}}{{\rm d}\rho_0}\vert_{\rm eq}$
Effective mass – SHF:	$\frac{\hbar^2}{2m^*}$	$=$	$\frac{\hbar^2}{2m} + \frac{\partial}{\partial\tau_0} \frac{E}{A}\vert_{\rm eq}$
Effective mass – RMF:	m^*	$=$	$m + G_\sigma \rho_{\rm S}$
TRK enhancement:	$\kappa_{\rm TRK}$	$=$	$\frac{m}{m^*} - 1 + \frac{1}{2}\rho_0 \frac{\rm d}{{\rm d}\rho_1} \frac{m}{m_n^*}$

3.1 Nuclear matter properties

Bulk properties of symmetric nuclear matter, called nuclear matter properties (NMP), are often used to characterize the properties of a model, or functional respectively. Starting point for the definition of NMP is the binding energy per nucleon in the symmetric nuclear matter $E/A = E/A(\rho_0, \rho_1, \tau_0, \tau_1)$. Variation with respect to Kohn-Sham wave functions establishes a relation $\tau_i = \tau_i(\rho_0, \rho_1)$ between kinetic densities τ_i and densities ρ_i. This yields the commonly used binding energy at equilibrium, $E/A[\rho_0, \rho_1, \tau_0(\rho_0, \rho_1), \tau_1(\rho_0, \rho_1)]$, as a function of the densities ρ_i alone. Table 2 lists the NMP discussed in this work. We consider τ_i as independent variables for the purpose of a formally compact definition of the effective mass in SHF. This is indicated by the partial derivatives with respect to τ_i for m^*/m in SHF and $\kappa_{\rm TRK}$. Static properties are deduced from the binding energy at equilibrium, which depends on ρ_i only. This is indicated by using the total derivatives for K_∞, $a_{\rm sym}$, and L. The slope of the symmetry energy L parametrizes the density dependence of $a_{\rm sym}$. This quantity is essential for the characterization of the EOS of neutron matter and the mass-radius relation in neutron stars [34–39]. The notion of effective mass is ambiguous in RMF. In this survey, we have decided to use what is called the Dirac mass. (Alternatively, one can talk about the effective mass at the Fermi surface, which is typically 10% larger than the Dirac mass.) The Thomas-Reiche-Kuhn (TRK) enhancement factor $\kappa_{\rm TRK}$ [40] is merely used to characterize the isovector effective mass. (The alternative value deduced from the mass at the Fermi momentum is typically 20% smaller.) The quantity m_n^* is the neutron effective mass. It is defined in the same way as the isoscalar effective mass m^* but using the derivative with respect to the neutron kinetic density τ_n.

Next to NMP come the corresponding bulk surface parameter, the (isoscalar) surface energy $a_{\rm surf}$ and the (isovector) surface symmetry energy $a_{\rm ssym}$. These surface parameters can be determined from the leptodermous expansion of the liquid drop model (LDM) energy per nucleon, $\mathcal{E}_{\rm LDM} = E_{\rm LDM}/A$, in terms of inverse radius

($\propto A^{-1/3}$) and neutron excess I [41],

$$\mathcal{E}_{\mathrm{LDM}}(A,I) = a_{\mathrm{vol}} + a_{\mathrm{surf}}A^{-1/3} + a_{\mathrm{curv}}A^{-2/3} + a_{\mathrm{sym}}I^2 + a_{\mathrm{ssym}}A^{-1/3}I^2 + a^{(2)}_{\mathrm{sym}}I^4. \quad (7)$$

The LDM energy $\mathcal{E}_{\mathrm{LDM}}(A,I)$ is obtained from the DFT calculation by subtracting the fluctuating shell correction energy. The general strategy behind this correction and leptodermous expansion is detailed in refs. [41,42]. In essence, we combine NM calculations ($A=\infty$) with (shell-corrected) DFT calculations for a huge set of spherical nuclei and extract the surface parameters by a fit to the expansion (7). Alternatively and simpler, one can compute the surface energy and surface symmetry energy through a semi-classical approximation (extended Thomas-Fermi) for the semi-infinite nuclear matter [43]. In this paper, we shall apply both strategies, the semi-classical approach whenever RMF is involved.

An important parameter characterizing the pure neutron matter is the neutron pressure

$$P(\rho_n) = \rho_n^2 \frac{\mathrm{d}}{\mathrm{d}\rho_n}\left(\frac{E}{A}\right)_n, \quad (8)$$

a quantity that is proportional to the slope of the binding energy of neutron matter at a given neutron density (derivative of neutron EOS). As discussed below, P is excellent isovector indicator.

3.2 Observables from finite nuclei

The total energy of a nucleus $E(Z,N)$ is the most basic observable described by SCMF. It is also the most important ingredient for calibrating the functional, see sect. 4.1. We often consider binding energy differences. Of great importance for stability analysis are separation energies and Q_α values. Another energy observable, potentially useful in the context of NSE, is the indicator

$$\delta V_{pn} = -\frac{1}{4}[E(N,Z) - E(N-2,Z) - E(N,Z-2) + E(N-2,Z-2)], \quad (9)$$

involving the double difference of binding energies [44]. Since δV_{pn} approximates the mixed partial derivative of binding energy with respect to N and Z, for nuclei with an appreciable neutron excess, the average value of δV_{pn} probes the symmetry energy term of LDM [45]: $\delta V_{pn}^{\mathrm{LDM}} \approx 2(a_{\mathrm{sym}} + a_{\mathrm{ssym}}A^{-1/3})/A$. That is, the shell-averaged trend of δV_{pn} is determined by the symmetry and surface symmetry energy coefficients.

It has been shown in [46] that effective SCMF provide a pertinent description of the form factors in the momentum regime $q < 2q_{\mathrm{F}}$ where q_{F} is the Fermi momentum. The key features of the nuclear density are related to this low-q range. The basic parameters characterizing nuclear density distributions are: r.m.s. charge radius r_{C}, diffraction radius R_{C}, and surface thickness σ_{C} [47]. The diffraction radius R_{C}, also called the box-equivalent radius, parametrizes the gross diffraction pattern which resemble those of a hard sphere of radius R_{C} [47]. The actual charge form factor $F_{\mathrm{C}}(q)$ falls off faster than the box-equivalent form factor F_{box}. This is due to the finite surface thickness σ which, in turn, can be determined by comparing the height of the first maximum of F_{box} with F_{C} from the realistic charge distribution. The charge halo parameter h_{C} is composed from the three basic charge form parameters and serves as a nuclear halo parameter found to be a relevant measure of the outer surface diffuseness [48].

The charge distribution is basically a measure of the proton distribution. It is only recently that the parity-violating electron scattering experiment PREX has provided some information on the weak-charge form factor $F_W(q)$ of ^{208}Pb [49,50]. These unique data gives access to neutron properties, such as the neutron r.m.s. radius r_{n}. Closely related and particularly sensitive to the asymmetry energy is the neutron skin $r_{\mathrm{skin}} = r_{\mathrm{n}} - r_{\mathrm{p}}$, which is the difference of neutron and proton r.m.s. radii. (As discussed in ref. [48], it is better to define the neutron skin through neutron and proton diffraction radii and surface thickness. However, for well-bound nuclei, which do not exhibit halo features, the above definition of r_{skin} is practically equivalent.) Neutron radii and skins are excellent isovector indicators [14,36,51–57] that help to check and improve isovector properties of the nuclear EDF [14].

Nuclear excitations are characterized by the strength distributions $S_{JT}(E)$ where J is the angular momentum of the excitation, T its isospin, and E the excitation energy. For example, the cross section for photo-absorption is proportional to $S_{11}(E)$. The strengths functions can be obtained from the excitation spectrum,

$$S_{JT}(E) = \sum_n E_n B_n(EJT)\delta_\Delta(E-E_n), \quad (10)$$

where E_n is the excitation energy of state n, $B_n(EJT)$ the corresponding transition matrix element of multipolarity J and isospin T, and δ_Δ as finite width folding function —if $S_{JT}(E)$ is calculated theoretically using, *e.g.*, the random phase approximation (RPA). In our RPA estimates, we use an energy-dependent width $\Delta = \max(\Delta_{\min}, (E_n - E_{\mathrm{thr}})/E_{\mathrm{slope}})$ which simulates the broadening mechanisms beyond RPA. The parameters for ^{208}Pb are $\Delta_{\min} = 0.2\,\mathrm{MeV}$, $E_{\mathrm{thr}} = 10\,\mathrm{MeV}$, and $E_{\mathrm{slope}} = 5\,\mathrm{MeV}$. The resulting spectral distributions for heavy nuclei, as ^{208}Pb, show one clear giant resonance peak at $E_{\mathrm{GR}}(JT)$ for $(J,T) = (0,0), (1,1), (2,0)$. We will consider these resonance energies as characteristic observables of dynamical response in heavy nuclei. The strength functions $S_{JT}(E)$ in light nuclei are much more fragmented and cannot be reduced to one single characteristic number.

There are other key observables that can be extracted from the strength distributions. In particular, for the dipole case $S_{11}(E)$, a key observable is the electric dipole polarizability,

$$\alpha_{\mathrm{D}} = \sum_n E_n^{-1} B_n(E11). \quad (11)$$

In the following, we will consider $\alpha_{\rm D}$ for ^{208}Pb. It has been demonstrated [14,57] that $\alpha_{\rm D}$ strongly correlates with NSE; hence, it can serve as excellent isovector indicator that can be precisely extracted from measured $E1$ strength [58]. On the other hand, the low-energy $E1$ strength, sometimes referred to as the pygmy dipole strength, exhibits weak collectivity. The correlation between the accumulated low-energy strength and the symmetry energy is weak, and depends on the energy cutoff assumed [14,59,60].

Giant resonances are small amplitude excitations and belong to the regime of linear response. The low-energy branch of isoscalar quadrupole excitations is often associated with large amplitude collective motion along nuclear shapes with substantial quadrupole deformation. Of particular importance is nuclear fission, which determines existence of heavy and superheavy nuclei. As a simple and robust measure of fission, we shall consider the axial fission barrier height in ^{266}Hs. Unlike actinides, most superheavy nuclei have one single fission barrier [61–63], which simplifies the analysis for our purpose. It has to be kept in mind that the inner barrier is often lowered by triaxial shapes, but this is not important for the study of large-amplitude nuclear deformability.

4 Symmetry energy: constraints and correlations

4.1 Brief review of χ^2 technique and correlation analysis

As discussed in sect. 2, the nuclear EDF is characterized by about a dozen of coupling constants $\mathbf{p} = (p_1, \ldots, p_F)$ that are determined by confronting DFT predictions with experiment. The standard procedure is to adjust the parameters $\mathbf{p}$ to a large set of nuclear observables in carefully selected nuclei [5,17,18,64,65]. This is usually done by the standard least-squares optimization technique. The starting point is the χ^2 objective function

$$\chi^2(\mathbf{p}) = \sum_{\mathcal{O}} \left(\frac{\mathcal{O}^{(\rm th)}(\mathbf{p}) - \mathcal{O}^{(\rm exp)}}{\Delta\mathcal{O}} \right)^2, \qquad (12)$$

where “th” stands for the calculated values, “exp” for experimental data, and $\Delta\mathcal{O}$ for adopted errors. The optimum parametrization $\mathbf{p}_0$ is the one which minimizes χ^2 with the minimum value $\chi_0^2 = \chi^2(\mathbf{p}_0)$. Around the minimum $\mathbf{p}_0$, there is a range of “reasonable” parametrizations $\mathbf{p}$ that can be considered as delivering a good fit, *i.e.*, $\chi^2(\mathbf{p}) \leq \chi_0^2 + 1$. As this range is usually rather small, we can expand χ^2 as

$$\chi^2(\mathbf{p}) - \chi_0^2 \approx \sum_{i,j=1}^{F} (p_i - p_{i,0}) \mathcal{M}_{ij} (p_j - p_{j,0}), \qquad (13)$$

$$\mathcal{M}_{ij} = \tfrac{1}{2} \partial_{p_i} \partial_{p_j} \chi^2 |_{\mathbf{p}_0}. \qquad (14)$$

The reasonable parametrizations thus fill the confidence ellipsoid given by

$$(\mathbf{p} - \mathbf{p}_0) \hat{\mathcal{M}} (\mathbf{p} - \mathbf{p}_0) \leq 1, \qquad (15)$$

see sect. 9.8 of [66]. Given a set of parameters $\mathbf{p}$, any observable $A = \langle \hat{A} \rangle$ can be uniquely computed. In this way, $A = A(\mathbf{p})$. The value A thus varies within the confidence ellipsoid, and this results in some uncertainty ΔA. Let us assume for simplicity that the observable varies weakly with $\mathbf{p}$ such that one can linearize in the relevant range $A(\mathbf{p}) = A_0 + (\mathbf{p} - \mathbf{p}_0) \cdot \boldsymbol{\partial}_{\mathbf{p}} A$. Let us, furthermore, associate a weight $\propto \exp(-\chi^2(\mathbf{p}))$ with each parameter set. A weighted average over the parameter space yields the covariance between two observables $\hat{A}$ and $\hat{B}$, which represents their combined uncertainty,

$$\overline{\Delta A\, \Delta B} = \sum_{ij} \partial_{p_i} A (\hat{\mathcal{M}}^{-1})_{ij} \partial_{p_j} B. \qquad (16)$$

For $A = B$, eq. (16) gives the variance $\overline{\Delta^2 A}$ that defines a statistical uncertainty of an observable. Variance and covariance are useful quantities that allow to estimate the impact of an observable on the model and its parametrization. We shall explore the covariance analysis in three different ways,

1) We perform a constrained fit during which the observable of interest is kept fixed at a desired value. In the present paper, we consider the symmetry energy $a_{\rm sym}$ as constraining observable. Comparing uncertainties from a constrained fit with those from an unconstrained fit provides a first indicator on the impact of the constrained observable on other observables.
2) The next step is a trend analysis, in which one performs a series of constrained fits with systematically varied values of the constraining observable. One then studies other observables as a function of the constrained quantity. This provides valuable information on possible inter-dependences.
3) Finally, we compute correlation (16) between $a_{\rm sym}$ and other observables. Here, a useful dimensionless measure is given by the Pearson product-moment correlation coefficient [66],

$$c_{AB} = \frac{|\overline{\Delta A\, \Delta B}|}{\sqrt{\overline{\Delta A^2}\; \overline{\Delta B^2}}}. \qquad (17)$$

A value $c_{AB} = 1$ means fully correlated and $c_{AB} = 0$ – uncorrelated.

In the following, we will apply these three ways of studying correlations with $a_{\rm sym}$ to different groups of observables. To this end, we have produced a series of parametrizations with systematically varied $a_{\rm sym}$ for the SV Skyrme family and for the RMF-ME and RMF-PC models.

The optimization and covariance analysis carried out in this survey for all three EDFs (SHF-SV, RMF-PC, and RMF-ME) is based on the same standard set of data on spherical nuclei (masses, diffraction radii, surface thickness, charge radii, separation energies, isotope shifts, and odd-even mass differences) that has originally been proposed in ref. [17] and recently employed in refs. [67,38]. We wish to emphasize that this is the first time that one consistent phenomenological input has been used to constrain SHF and RMF EDFs. A slightly modified variant of the fitting protocol has been used for RMF-ME. This EDF did not lead to stable results in the fits which were unconstrained by NMP. Consequently, we included the nuclear matter information on $(E/A)_{\mathrm{eq}}$ into the dataset. This is still much less than in the previously published optimization protocols of RMF-ME, in which all NMP were constrained [28,29,68].

4.2 Correlations with nuclear matter properties

The NMP corresponding to unconstrained optimization of SHF-SV, RMF-PC, and RMF-ME EDFs —using the same standard dataset— are shown in table 3. They are compared with NMP of SHF-RD [67] (employing a modified density dependence and the standard dataset) and SHF-TOV [38] (using neutron star data in addition the standard dataset in the optimization process). As expected, isoscalar effective mass is significantly lowered in RMF as compared to SHF, and the opposite holds for κ_{TRK}. The slope parameter L is predicted to be very different in all five models. In particular, RMF-ME has very low value of L, and —at the same time— the uncertainty on a_{sym} in this model is very small.

Figure 1 shows the trends for selected properties of symmetric nuclear matter with a_{sym}. The purpose of this analysis is to relate systematic variations with a_{sym} to statistical uncertainties. The isoscalar properties K_∞, m^*/m as well as the isovector dynamical response κ_{TRK} are fairly insensitive to a_{sym}. Their variation with a_{sym} are much smaller than the typical statistical uncertainties. This independency is also indicated by the fact that the uncertainty obtained in the unconstrained fit is not visibly larger than those from the constrained optimizations. The trend is markedly different for the density dependence of the symmetry energy L: variations with a_{sym} well exceed the statistical error bars and the uncertainties from unconstrained fits are larger than those from constrained calculations. It is to be noted that the dedicated variations of a_{sym} stay within the uncertainty of a_{sym} in the unconstrained optimization. The uncertainty of L in the free fit thus covers nicely the uncertainty of the constrained calculations plus the variation of L with a_{sym}. Anyway, the results shows that L cannot be used as independent NMP although the formal structure of the EDF would allow that. There seems to be a strong link established by the data which yet has to be worked out.

4.3 Correlations with properties of finite nuclei

Figure 2 illustrates the trends with a_{sym} and extrapolation uncertainties for three observables in ^{208}Pb: weak-charge form factor at $q = 0.475\,\mathrm{fm}^{-1}$ (q-value of PREX), neutron skin, and dipole polarizability. These observables are all known to be sensitive to isovector properties of EDF [14,57]. This is confirmed by the trends in the present results. The comparison of uncertainties shows a large growth when going from constrained to unconstrained optimizations. This corroborates the close relation between the symmetry energy and the three isovectors indicators shown in fig. 2. It is, furthermore, interesting to note that SHF and RMF-PC stay safely within the bands given by experimental data and RMF-ME is not far away. A better discrimination between models requires more precise data, a task on which presently many experimental groups are heavily engaged.

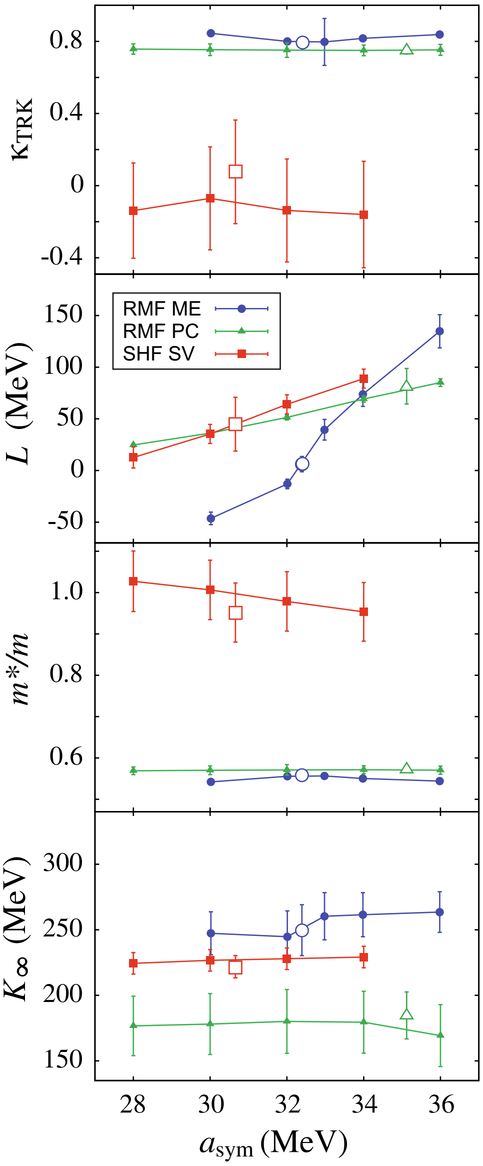

Fig. 1. Behavior of selected nuclear matter properties with symmetry energy a_{sym} for the SV Skyrme family and for the ME and PC RMF model families. The statistical uncertainties are indicated by error bars. The result of the unconstrained fits are shown by large open symbols with corresponding error bars.

Table 3. Nuclear matter parameters of SHF-SV, RMF-PC, and RMF-ME EDFs used in this paper (with error bars) obtained by means of unconstrained optimization. Also shown are the values of NMP of SHF-RD [67] and SHF-TOV [38].

Model	ρ_{eq} (fm^{-3})	E/A (MeV)	K_∞ (MeV)	m^*/m	a_{sym} (MeV)	L (MeV)	κ_{TRK}
SHF-SV	0.161(1)	−15.91(4)	222(9)	0.95(7)	31(2)	45(26)	0.08(29)
RMF-PC	0.159(1)	−16.14(3)	185(18)	0.57(1)	35(2)	82(17)	0.75(2)
RMF-ME	0.159(3)	−16.2(2)	250(19)	0.56(1)	32.4(1)	6(7)	0.79(2)
SHF-RD	0.161	−15.93	231	0.90	32(2)	60(32)	0.04(32)
SHF-TOV	0.161	−15.93	222	0.94	32(1)	76(15)	0.21(26)

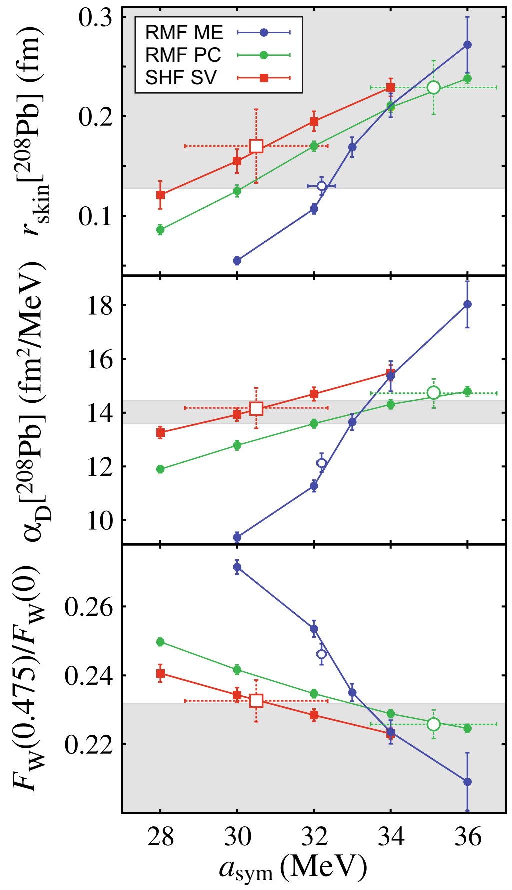

Fig. 2. Similar to fig. 1, but for selected properties of ^{208}Pb: neutron skin (top), dipole polarizability (middle), and weak-charge form factor (bottom). The current experimental ranges are shaded grey: $r_{\text{skin}} = 0.33^{+0.16}_{-0.18}$ fm [49], $\alpha_D = 14.0 \pm 0.4$ fm^2/MeV [58], and $F_W(0.475)/F_W(0) = 0.204 \pm 0.028$ [50].

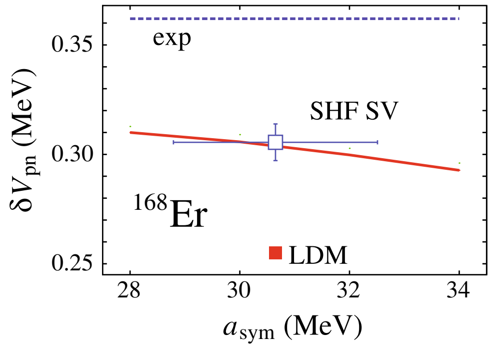

Fig. 3. Behavior of δV_{pn} in ^{168}Er with symmetry energy a_{sym} for SHF-SV (solid line) as compared to experiment (dashed line) and the LDM value (filled square). The result of the unconstrained fit is marked by a large open square with corresponding error bars.

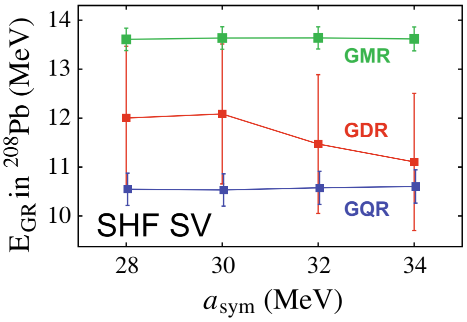

Fig. 4. Behavior of giant resonance energies in ^{208}Pb with symmetry energy a_{sym} for the SV Skyrme family [17]. In order not to make the graph too busy the uncertainties from the unconstrained fit are not shown; they have the same size as those from the constrained fits.

To explore the usefulness of δV_{pn} as an isovector indicator, we choose the heavy deformed nucleus ^{168}Er, as its even-even neighbors have similar structure and the calculated values of δV_{pn} for even-even Er isotopes show little variations around $N = 100$. The results displayed in fig. 3 show a gradual decrease of this quantity with a_{sym}, but the magnitude of the variation is very small and cannot account for the deviation from experiment (around 50 keV). It is apparent that this quantity is too strongly influenced by shell effects (given by the deviation from the LDM estimate; also around 50 keV) to probe NSE, see refs. [45, 69] and sect. 4.4 below.

Figure 4 shows the trends of the three major giant resonances in ^{208}Pb: isoscalar monopole resonance (GMR), isovector dipole resonance (GDR), and isoscalar quadrupole resonance (GQR). For technical reasons, we only show results obtained with the SV Skyrme family. The isoscalar resonances show no dependence on a_{sym} at all; this is understandable for the symmetry energy belongs to the isovector sector. Somewhat surprisingly, the GDR exhibits very little dependence on a_{sym} as well, with

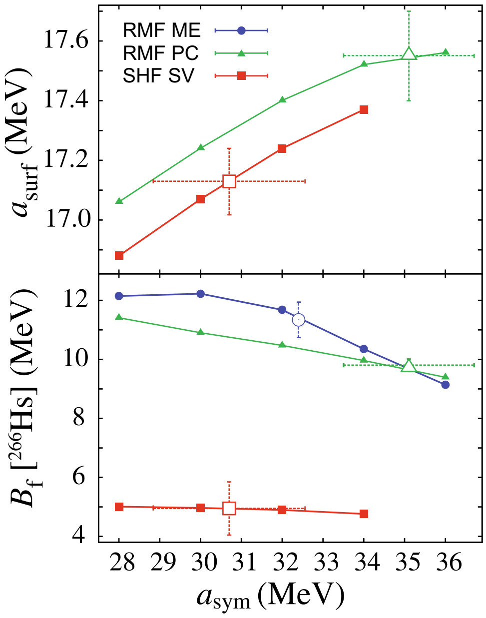

Fig. 5. Similar to fig. 1, but for surface energy (top) and fission barrier (bottom) in ^{266}Hs. The surface energy from RMF-ME is not shown.

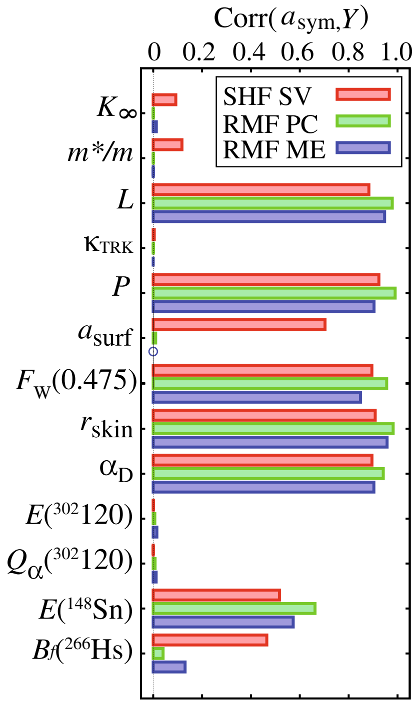

Fig. 6. The correlation (17) between symmetry energy and selected observables (Y) for three models: SHF-SV, RMF-PC and RMF-ME. Results correspond to unconstrained optimization employing the same strategy in all three cases. For RMF-ME no reliable numbers could be obtained for a_{surf}; this is indicated by an open circle.

the magnitude of variations well below the statistical uncertainties. As demonstrated earlier [17,57], it is the sum-rule enhancement factor κ_{TRK} that has the dominant impact on the GDR peak frequency rather than a_{sym}. The covariance analysis of fig. 4 confirms that the energies of GMR, GDR, and GQR do not obviously relate to a_{sym}.

Figure 5 shows behavior of surface energy a_{surf} and the inner fission barrier B_f in ^{266}Hs with a_{sym}. The surface energy was computed by means of the extended Thomas-Fermi method. (The surface energy from RMF-ME is not shown: we do not have at our disposal a code for semi-infinite matter which could handle this particular RMF functional.) The trends of a_{surf} predicted by SHF and RMF are similar. An offset of about 2 MeV is most likely due to very different effective masses in both models. Much larger differences are seen for the fission barriers. The basic difference between SHF and RMF can again be explained predominantly in terms of effective masses. Barriers are produced by shell effects and shell effects are larger for lower effective masses. There is also a difference between the two RMF models. This could be due to a different handling of gradient terms (only RMF-PC contains such) and a much different parametrization of density dependence. All three models show not only different values as such, but also different trends.

The statistical errors differ substantially between the models. RMF-ME shows a small uncertainty in B_f. This may be due to the missing gradient term in this model which would also restrict the uncertainty in the surface energy. We note, however, that the gradient term in RMF-PC is to a certain extent equivalent the mass term of the sigma meson in RMF-ME, which is considered a free parameter. The plot of the B_f demonstrates nicely the relative role of statistical and systematic errors, with the statistical errors being much smaller than inter-model differences. As discussed in refs. [70,42], fission barriers are strongly affected by a_{surf} and a_{ssym} of EDF. In particular, the recently developed EDF UNEDF1, suitable for studies of strongly elongated nuclei, has relatively low values of a_{surf} and a_{ssym} (see fig. 7 below) that reflect the constraints on the fission isomer data. The reduced surface energy coefficients result in a reduced effective surface coefficient $a_{\mathrm{surf}}^{(\mathrm{eff})} = a_{\mathrm{surf}} + a_{\mathrm{ssym}} I^2$, which has profound consequences for the description of fission barriers, especially in the neutron-rich nuclei that are expected to play a role at the final stages of the r-process through the recycling mechanism [71].

4.4 Correlations summary

The summary of our correlation analysis for a_{sym} is given in fig. 6. The first four entries concern the same nuclear matter properties as in fig. 1. It is only for L, the slope of symmetry energy, that a strong correlation with a_{sym} is seen. This complies nicely with the findings of the trend analysis in fig. 1. The next entry concerns the neutron pressure (8) at $\rho_n = 0.08\,\mathrm{neutrons/fm}^3$. It is also strongly correlated with a_{sym}, which is no surprise because it is an excellent isovector indicator [14,36,53,54,72,73]. The diagram shows, furthermore, the (isoscalar) surface energy a_{surf} computed in semi-classical approximation. This quantity is well correlated with a_{sym} for SHF and practically uncorrelated for RMF.

The next three entries are observables in ^{208}Pb: weak-charge form factor, neutron skin, and dipole polarizability. All three are known to be strong isovector indicators [14, 57,36]. This is confirmed here for all three models.

The remaining four entries deal with exotic nuclei. These are: binding energy and α-decay energy in yet-to-be-measured superheavy nucleus $Z = 120$, $N = 182$, binding energy in an extremely neutron rich ^{148}Sn, and the fission barrier in ^{266}Hs (for which trends had been shown already in fig. 5). The data on $Z = 120$, $N = 182$ consistently do not correlate with a_{sym}. The binding energy of ^{148}Sn shows some correlation with a_{sym}, about equally strong in the three models. This is expected as a large neutron excess surely explores the static isovector sector. Finally, the correlation with fission barrier in ^{266}Hs exhibits an appreciable model dependence with some correlation in SHF and practically none in RMF.

We also studied correlations between δV_{pn} in ^{168}Er and other observables for finite nuclei and NM. We did not find a single observable that would correlate well with this binding-energy indicator. In particular, the correlation coefficient (17) with a_{sym} is 0.41, with α_{D} in ^{208}Pb is 0.6, and with r_{skin} in ^{208}Pb is 0.54. This results demonstrates that δV_{pn} in one single nucleus is too strongly influenced by shell effects to be used as an isovector indicator.

5 Symmetry energy parameters of EDFs

The actual values of symmetry energy parameters depend on i) the form of EDF and ii) the optimization strategy used. The first point is nicely illustrated in table 3, which compares NMP for different functional forms (SHF-SV, SHF-RD, RMF-PC, and RMF-ME) using the same dataset and the same optimization technique. As far as the second point, it is instructive to compare SHF-SV and SHF-TOV NMP; namely, the inclusion of additional data on neutron stars in SHF-TOV has significantly impacted L and κ_{TRK}. Many other examples can be found in refs. [19,74] that demonstrate divergent predictions of Skyrme EDFs for neutron and nuclear matter.

The range of a_{sym} is fairly narrowly constrained by various data and *ab initio* theory [34]; it is $28\,\mathrm{MeV} < a_{\mathrm{sym}} < 34\,\mathrm{MeV}$. The recent Finite-Range Droplet Model (FRDM) result [75] is $a_{\mathrm{sym}} = 32.5 \pm 0.5\,\mathrm{MeV}$. All EDFs listed in table 3 are consistent with these expectations.

The values of L are less precisely determined [34–39, 76–79]; there is more dependence on specific observables or methodology used. Recent surveys [34,39] suggest that a reasonable range of L is $40\,\mathrm{MeV} < L < 80\,\mathrm{MeV}$, and FRDM gives $L = 70 \pm 15\,\mathrm{MeV}$ [75]. Except for RMF-ME, all models shown in table 3 are consistent with these estimates. The low value of L in RMF-ME is troublesome; here we note that while SHF-SV and RMF-PC EDFs fall within the error bars of the current experimental data in fig. 2, RMF-ME (as defined by the present optimization protocol) does not. In this context, it is worth mentioning that in the case of RMF-ME the objective function is very steep in the direction of a_{sym}. This is seen in table 3, which shows the uncertainties of a_{sym} for the three models employed. Consequently, the RMF-ME results are mostly in a sub-optimal range of the model in a broad range of a_{sym}. For instance, at $a_{\mathrm{sym}} = 30\,\mathrm{MeV}$, the average deviation for binding energies with RMF-ME is about twice as large as for the optimal value $a_{\mathrm{sym}} = 32.4\,\mathrm{MeV}$.

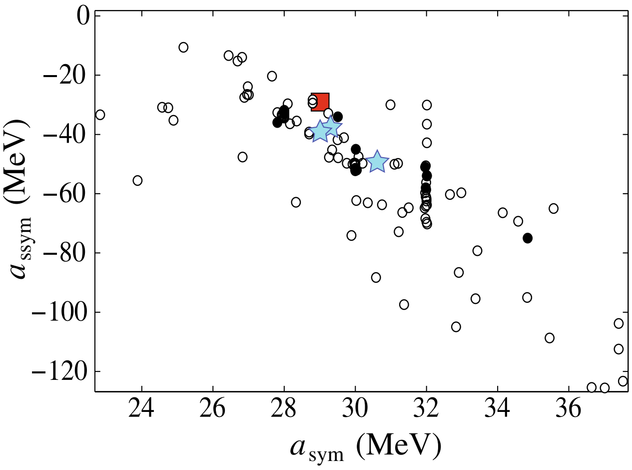

Fig. 7. Correlation between the symmetry and surface symmetry coefficients taken from ref. [70] (Skyrme EDFs, dots; LDM values, stars) and ref. [81] (Skyrme EDFs, circles). The UNEDF1 values [42] are marked by a square. (Adopted from [70].)

As discussed in ref. [41], the leading surface and symmetry terms appear relatively similar within each family of EDFs, with a clear difference for a_{sym} between SHF and RMF. By averaging over Skyrme-EDF results of refs. [41,80], one obtains: $a_{\mathrm{sym}} \approx 30.9 \pm 1.7\,\mathrm{MeV}$, $a_{\mathrm{ssym}} \approx -48 \pm 10\,\mathrm{MeV}$. Older relativistic models provide systematically larger values [41]: $a_{\mathrm{sym}} \approx 40.4 \pm 2.7\,\mathrm{MeV}$ and $a_{\mathrm{ssym}} \approx -103 \pm 18\,\mathrm{MeV}$. (Codes for a leptodermous expansion of the recent RMF-PC and RMF-ME models have yet to be developed.)

The coefficient a_{ssym} is poorly constrained in the current EDF parameterizations and there are large differences between models, see fig. 7. In addition, the values of a_{sym} and a_{ssym} have been shown to be systematically (anti)correlated [51,70,81,82]. Figure 7, displays the pairs $(a_{\mathrm{sym}}, a_{\mathrm{ssym}})$ for various Skyrme EDFs and LDM parametrizations. While a correlation between a_{sym} and a_{ssym} is apparent, a very large spread of values is seen that demonstrates that the data on g.s. nuclear properties are not able to constrain a_{ssym}. It is interesting to note that the LDM values and phenomenological estimates cluster around $a_{\mathrm{sym}} = 30\,\mathrm{MeV}$ and $a_{\mathrm{ssym}} = -45\,\mathrm{MeV}$. The values for UNEDF1 functional, additionally constrained by the data on very deformed fission isomers (thus probing the surface-isospin sector of EDF) are $a_{\mathrm{sym}} = 29\,\mathrm{MeV}$ and $a_{\mathrm{ssym}} = -29\,\mathrm{MeV}$.

6 Isospin physics and symmetry energy

The emergence of NSE is rooted in the isobaric symmetry and its breaking as a function of neutron excess and mass. Single-reference DFT is essentially the only framework allowing for understanding global behavior of isospin effects throughout the entire nuclear landscape. While the nuclear interaction part of the nuclear EDF is constructed to be an isoscalar [24,25], the Coulomb interaction breaks isospin manifestly. There are, therefore, two different sources of isospin symmetry breaking in the nuclear DFT: spontaneous isospin breaking associated with the self-consistent response to the neutron excess, and the explicit breaking due to the electric charge of the protons [83].

Effects related to isospin breaking and restoration are difficult to treat theoretically within the nuclear DFT. Below, we discuss two ways of dealing with this problem: isocranking and isospin projection.

6.1 1D and 3D isocranking

The isocranking model [84,80] attributes the kinetic coefficient $a_{\rm sym,kin}$ contribution to the mean level spacing at the Fermi energy $\varepsilon(A)$ rather than to the total kinetic energy itself. The SHF calculations also revealed that the isovector mean potential of the Skyrme EDF can be quite well characterized by an effective V_{TT} interaction (1) characterized by a strength parameter $\kappa(A)$. The actual isovector part of the Skyrme mean-field potential is composed of several terms [24,25]. As can be seen from table 1, in the uniform NM limit, two terms contribute in SHF, $C_1^\rho \rho_1^2$ and $C_1^\tau \rho_1 \tau_1$, and the NSE strength reads

$$a_{\rm sym} = \frac{1}{8}\frac{m}{m^*}\varepsilon_{FG} + \left[\left(\frac{3\pi^2}{2}\right)^{2/3} C_1^\tau \rho_0^{5/3} + C_1^\rho \rho_0\right], \quad (18)$$

where $\varepsilon_{\rm FG}$ is the average level splitting in FGM. Therefore, within this scenario, $a_{\rm sym}$ is non-trivially modified by momentum-dependent effects introducing, in the leading order, the dependence of $a_{\rm sym,kin}$ and $a_{\rm sym,int}$ on the isoscalar and isovector effective mass, respectively.

Within the nuclear shell model, NSE appears through a contribution to the binding energy proportional to $T(T+1)$ [85]. However, the local enhancement of binding around $N = Z$ (the Wigner energy) suggest an enhancement of the linear term to $T(T+\lambda)$ with $\lambda \approx 1.26$ [86–88]. Since the Wigner energy is neither fully understood nor included properly within the SCMF models [89], the microscopic origin of λ is still a matter of debate. Within the isocranking model, the Fock exchange (isovector) potential gives rise to $\lambda \approx 0.5$, at variance with enhancement seen in experimental data. The Wigner energy can be explained by shell-model calculations [89] in terms of configuration mixing. The Wigner term is usually associated with the isoscalar neutron-proton (np) pairing [90,25], but its understanding is poor as realistic calculations involving simultaneous np mixing in both the particle-hole (p-h) and particle-particle (p-p) channels have not been carried out. It is only very recently that 3D isocranking calculations including np mixing in the p-h channel have been reported [91]. This is the first step towards developing the nuclear superfluid DFT including np mixing in both p-h and p-p channels. An improved treatment of isospin within the 3D isocranking will open new opportunities for quantitative studies of isobaric analogue states and, in turn, the NSE.

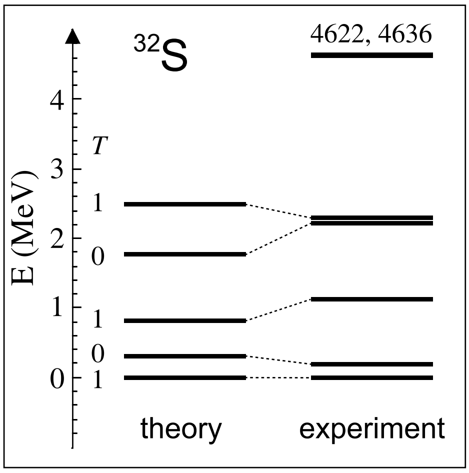

Fig. 8. Energies of $I^\pi = 1^+$ states in ^{32}S normalized to the isobaric analogue state $I^\pi = 1^+, T = 1$. The results of projected SHF-SkV calculations involving configuration mixing [94] (left) are compared to experiment (right). The calculations are based on 24 $I = 1^+$ states projected from 6 HF determinants representing low-lying 1p-1h configurations.

6.2 Isospin projected DFT

The isospin and isospin-plus-angular-momentum projected DFT models have been developed recently to describe isospin mixing effects. These new tools open new avenues to probe NSE. To gain insight on this line of models, it is instructive to to consider the spontaneous isospin symmetry breaking effect in the so-called anti-aligned p-h configurations in $N = Z$ nuclei, which are mixtures of $T = 0$ and $T = 1$ states [92]. Restoration of the isospin symmetry results in the energy splitting, ΔE_T, between the actual $T = 0$ and $T = 1$ configurations. Since these states are projected from a single mean-field determinant, the splitting is believed to be insensitive to kinematics, and the method can be used to probe dynamical effects giving rise to the interaction term $a_{\rm sym,int}$. The results of SHF calculations [92] performed in finite nuclei confirm that $a_{\rm sym,int}$ is indeed correlated with the isoscalar effective mass in agreement with the NM relation (18).

The isospin and isospin plus angular momentum projected DFT were designed and applied to study the isospin impurities [83] and isospin symmetry breaking corrections to the superallowed $0^+ \to 0^+$ β-decay rates [93]. Unfortunately, the calculations show that these two observables are not directly correlated with the symmetry energy. Ambiguities associated with these calculations stimulated further development of the formalism in the direction of the Resonating-group method. The scheme proceeds in three steps. i) First, a set of low-lying (multi)p-(multi)h SHF states $\{\Phi_i\}$ is calculated. These states form a basis for a subsequent projection. ii) Next, the projection techniques are applied to calculate a family $\{\Psi_I^{(\alpha)}\}$ of good angular momentum states with properly treated K-mixing and isospin mixing. iii) Finally, a configuration mixing of $\{\Psi_I^{(\alpha)}\}$ states is performed using techniques suitable for non-orthogonal ensambles.

Although at present the calculations can be realized only for the SkV EDF, the preliminary results [94] are encouraging, as shown in fig. 8. Since the projected approach treats rigorously the angular momentum conservation and the long-range polarization due to the Coulomb force, it opens up a possibility of detailed studies of the isovector terms of the nuclear EDF that are sources of the NSE.

7 Conclusions

This paper surveys various aspects of NSE within the nuclear DFT represented by non-relativistic and relativistic self-consistent mean-field frameworks. After defining the models and statistical tools, we reviewed key observables pertaining to bulk nucleonic matter and finite nuclei. Using the statistical covariance technique, constraints on the symmetry energy were studied, together with correlations between observables and symmetry energy parameters.

Through the systematic correlation analysis, we scrutinized various observables from finite nuclei that are accessible by current and future experiments. We confirm that by far the most sensitive isovector indicators are observables related to the neutron skin (neutron radius, diffraction radius, weak charge form factor) and the dipole polarizability [14,57]. In this context, PREX-II measurement of the neutron skin in ^{208}Pb [95] (a follow-up measurement to PREX [49] designed to improve the experimental precision), CREX measurement of the neutron skin in ^{48}Ca [96], and on-going measurements of α_D in neutron-rich nuclei [97] are indispensable.

The masses of heavy neutron-rich nuclei also seem to correlate well with NSE parameters. Other observables, such as Q_α-values, δV_{pn}, barrier heights, and low-energy dipole strength [14,59,60] are too strongly impacted by shell effects to be useful as *global* isovector indicators.

A major challenge is to develop the universal nuclear EDF with improved isovector properties. Various improvements are anticipated in the near future. Those include constraining the EDF at sub-saturation densities using *ab initio* models [98,99] and using the density matrix expansion to develop an EDF based on microscopic nuclear interactions [100]. This work will be carried out under the Nuclear Low Energy Computational Initiative (NUCLEI) [101]. Other exciting avenues are related to multi-reference isospin projected DFT, which will enable us to make reliable predictions for isobaric analogues, isospin mixing, and mirror energy differences.

This work was supported by the U.S. Department of Energy under Contract No. DE-FG02-96ER40963 (University of Tennessee), No. DE-SC0008499 (NUCLEI SciDAC Collaboration); by BMBF under Contract No. 06 ER 142D; and by NCN under Contract No. 2012/07/B/ST2/03907

References

1. P. Hohenberg, W. Kohn, Phys. Rev. **136**, B864 (1964).
2. W. Kohn, L. Sham, Phys. Rev. **140**, A1133 (1965).
3. D. Vautherin, D.M. Brink, Phys. Rev. C **5**, 626 (1972).
4. J.W. Negele, D. Vautherin, Phys. Rev. C **5**, 1472 (1972).
5. M. Bender, P.H. Heenen, P.G. Reinhard, Rev. Mod. Phys. **75**, 121 (2003).
6. J. Messud, M. Bender, E. Suraud, Phys. Rev. C **80**, 054314 (2009).
7. G.A. Lalazissis, P. Ring, D. Vretenar, *Extended Density Functionals in Nuclear Structure Physics*, Lecture Notes in Physics, Vol. **641** (Springer, 2004).
8. D. Vretenar, A.V. Afanasjev, G. Lalazissis, P. Ring, Phys. Rep. **409**, 101 (2005).
9. S. Weinberg, *The Quantum Theory of Fields*, Vols. **I-III** (Cambridge University Press, Cambridge, 1996-2000).
10. S. Puglia, A. Bhattacharyya, R. Furnstahl, Nucl. Phys. A **723**, 145 (2003).
11. B.G. Carlsson, J. Dobaczewski, M. Kortelainen, Phys. Rev. C **78**, 044326 (2008).
12. J. Drut, R. Furnstahl, L. Platter, Prog. Part. Nucl. Phys. **64**, 120 (2010).
13. J. Dobaczewski, K. Bennaceur, F. Raimondi, J. Phys. G **39**, 125103 (2012).
14. P.G. Reinhard, W. Nazarewicz, Phys. Rev. C **81**, 051303 (2010).
15. A. Bohr, B. Mottelson, *Nuclear Structure*, Vol. **I** (W. A. Benjamin, New York, 1969).
16. A.Z. Mekjian, L. Zamick, Phys. Rev. C **85**, 057303 (2012).
17. P. Klüpfel, P.G. Reinhard, T.J. Bürvenich, J.A. Maruhn, Phys. Rev. C **79**, 034310 (2009).
18. M. Kortelainen, T. Lesinski, J. Moré, W. Nazarewicz, J. Sarich, N. Schunck, M.V. Stoitsov, S. Wild, Phys. Rev. C **82**, 024313 (2010).
19. J. Stone, P.G. Reinhard, Prog. Part. Nucl. Phys. **58**, 587 (2007).
20. J. Erler, P. Klüpfel, P.G. Reinhard, J. Phys. G **38**, 033101 (2011).
21. J. Meng, H. Toki, S. Zhou, S. Zhang, W. Long, Prog. Part. Nucl. Phys. **57**, 470 (2006).
22. T. Nikšić, D. Vretenar, P. Ring, Prog. Part. Nucl. Phys. **66**, 519 (2011).
23. Y.M. Engel, D.M. Brink, K. Goeke, S.J. Krieger, D. Vautherin, Nucl. Phys. A **249**, 215 (1975).
24. E. Perlińska, S.G. Rohoziński, J. Dobaczewski, W. Nazarewicz, Phys. Rev. C **69**, 014316 (2004).
25. S.G. Rohoziński, J. Dobaczewski, W. Nazarewicz, Phys. Rev. C **81**, 014313 (2010).
26. P.G. Reinhard, Rep. Prog. Phys. **52**, 439 (1989).
27. T. Nikšić, D. Vretenar, P. Ring, Phys. Rev. C **78**, 034318 (2008).
28. T. Nikšić, D. Vretenar, P. Finelli, P. Ring, Phys. Rev. C **66**, 024306 (2002).
29. G.A. Lalazissis, T. Nikšić, D. Vretenar, P. Ring, Phys. Rev. C **71**, 024312 (2005).
30. P. Bonche, H. Flocard, P.H. Heenen, S.J. Krieger, M.S. Weiss, Nucl. Phys. A **443**, 39 (1985).
31. M. Bender, K. Rutz, P.G. Reinhard, J. Maruhn, Eur. Phys. J. A **8**, 59 (2000).
32. Y. Tian, Z. Ma, P. Ring, Phys. Lett. B **676**, 44 (2009).
33. Y. Tian, Z. Ma, P. Ring, Phys. Rev. C **80**, 024313 (2009).
34. J.M. Lattimer, Annu. Rev. Nucl. Part. Sci. **62**, 485 (2012).

35. M.B. Tsang *et al.*, Phys. Rev. C **86**, 015803 (2012).
36. F.J. Fattoyev, J. Piekarewicz, Phys. Rev. C **86**, 015802 (2012).
37. F.J. Fattoyev, W.G. Newton, J. Xu, B.A. Li, Phys. Rev. C **86**, 025804 (2012).
38. J. Erler, C.J. Horowitz, W. Nazarewicz, M. Rafalski, P.G. Reinhard, Phys. Rev. C **87**, 044320 (2013).
39. A.W. Steiner, J.M. Lattimer, E.F. Brown, Astrophys. J. **765**, L5 (2013).
40. P. Ring, P. Schuck, *The Nuclear Many-Body Problem* (Springer, 2000).
41. P.G. Reinhard, M. Bender, W. Nazarewicz, T. Vertse, Phys. Rev. C **73**, 014309 (2006).
42. M. Kortelainen, J. McDonnell, W. Nazarewicz, P.G. Reinhard, J. Sarich, N. Schunck, M.V. Stoitsov, S.M. Wild, Phys. Rev. C **85**, 024304 (2012).
43. D. Von-Eiff, J.M. Pearson, W. Stocker, M.K. Weigel, Phys. Lett. B **324**, 279 (1994).
44. J.Y. Zhang, R. Casten, D. Brenner, Phys. Lett. B **227**, 1 (1989).
45. M. Stoitsov, R.B. Cakirli, R.F. Casten, W. Nazarewicz, W. Satuła, Phys. Rev. Lett. **98**, 132502 (2007).
46. P.G. Reinhard, Phys. Lett. A **169**, 281 (1992).
47. J. Friedrich, N. Vögler, Nucl. Phys. A **373**, 192 (1982).
48. S. Mizutori, J. Dobaczewski, G. Lalazissis, W. Nazarewicz, P.G. Reinhard, Phys. Rev. C **61**, 044326 (2000).
49. PREX Collaboration (S. Abrahamyan *et al.*), Phys. Rev. Lett. **108**, 112502 (2012).
50. C.J. Horowitz *et al.*, Phys. Rev. C **85**, (2012).
51. F. Tondeur, M. Brack, M. Farine, J. Pearson, Nucl. Phys. A **420**, 297 (1984).
52. P.G. Reinhard, Nucl. Phys. A **649**, 305c (1999).
53. R. Furnstahl, Nucl. Phys. A **706**, 85 (2002).
54. S. Yoshida, H. Sagawa, Phys. Rev. C **69**, 024318 (2004).
55. B. Li, L. Chen, C. Ko, Phys. Rep. **464**, 113 (2008).
56. M. Warda, X. Viñas, X. Roca-Maza, M. Centelles, Phys. Rev. C **80**, 024316 (2009).
57. J. Piekarewicz, B.K. Agrawal, G. Colò, W. Nazarewicz, N. Paar, P.G. Reinhard, X. Roca-Maza, D. Vretenar, Phys. Rev. C **85**, 041302 (2012).
58. A. Tamii *et al.*, Phys. Rev. Lett. **107**, 062502 (2011).
59. I. Daoutidis, S. Goriely, Phys. Rev. C **86**, 034328 (2012).
60. P.G. Reinhard, W. Nazarewicz, Phys. Rev. C **87**, 014324 (2013).
61. J. Erler, K. Langanke, H.P. Loens, G. Martinez-Pinedo, P.G. Reinhard, Phys. Rev. C **85**, 025802 (2012).
62. A. Staszczak, A. Baran, W. Nazarewicz, Phys. Rev. C **87**, 024320 (2013).
63. M. Warda, J.L. Egido, Phys. Rev. C **86**, 014322 (2012).
64. F.J. Fattoyev, J. Piekarewicz, Phys. Rev. C **84**, 064302 (2011).
65. Y. Gao, J. Dobaczewski, M. Kortelainen, J. Toivanen, D. Tarpanov, Phys. Rev. C **87**, 034324 (2013).
66. S. Brandt, *Statistical and computational methods in data analysis* (Springer, New York, 1997) third English edition.
67. J. Erler, P. Klüpfel, P.G. Reinhard, Phys. Rev. C **82**, 044307 (2010).
68. S. Typel, H. Wolter, Nucl. Phys. A **656**, 331 (1999).
69. M. Bender, P.H. Heenen, Phys. Rev. C **83**, 064319 (2011).
70. N. Nikolov, N. Schunck, W. Nazarewicz, M. Bender, J. Pei, Phys. Rev. C **83**, 034305 (2011).
71. I. Panov, I.Yu.Korneev, F.K. Thielemann, Astron. Lett. **34**, 189 (2008).
72. B. Alex Brown, Phys. Rev. Lett. **85**, 5296 (2000).
73. S. Typel, B.A. Brown, Phys. Rev. C **64**, 027302 (2001).
74. M. Dutra, O. Lourenço, J.S. Sá Martins, A. Delfino, J.R. Stone, P.D. Stevenson, Phys. Rev. C **85**, 035201 (2012).
75. P. Möller, W.D. Myers, H. Sagawa, S. Yoshida, Phys. Rev. Lett. **108**, 052501 (2012).
76. B. Li, L. Chen, C. Ko, Phys. Rep. **464**, 113 (2008).
77. L. Trippa, G. Colò, E. Vigezzi, Phys. Rev. C **77**, 061304 (2008).
78. A. Steiner, S. Gandolfi, Phys. Rev. Lett. **108**, 081102 (2012).
79. F.J. Fattoyev, J. Piekarewicz, arXiv:nucl-th/1306.6034 (2013).
80. W. Satuła, R.A. Wyss, M. Rafalski, Phys. Rev. C **74**, 011301 (2006).
81. P. Danielewicz, J. Lee, Nucl. Phys. A **818**, 36 (2009).
82. M. Farine, J. Pearson, B. Rouben, Nucl. Phys. A **304**, 317 (1978).
83. W. Satuła, J. Dobaczewski, W. Nazarewicz, M. Rafalski, Phys. Rev. Lett. **103**, 012502 (2009).
84. W. Satuła, R.A. Wyss, Phys. Lett. B **572**, 152 (2003).
85. I. Talmi, Rev. Mod. Phys. **34**, 704 (1962).
86. J. Jänecke, Nucl. Phys. A **73**, 97 (1965).
87. J. Jänecke, T. O'Donnell, V. Goldanskii, Nucl. Phys. A **728**, 23 (2003).
88. S. Głowacz, W. Satuła, R. Wyss, Eur. Phys. J. A **19**, 33 (2004).
89. W. Satuła, D. Dean, J. Gary, S. Mizutori, W. Nazarewicz, Phys. Lett. B **407**, 103 (1997)
90. W. Satuła, R. Wyss, Phys. Lett. B **393**, 1 (1997).
91. K. Sato, J. Dobaczewski, T. Nakatsukasa, W. Satuła, RIKEN Accel. Prog. Rep., **46** (2013) arXiv:1308.1997.
92. W. Satuła, J. Dobaczewski, W. Nazarewicz, M. Borucki, M. Rafalski, Int. J. Mod. Phys. E **20**, 244 (2011).
93. W. Satuła, J. Dobaczewski, W. Nazarewicz, M. Rafalski, Phys. Rev. Lett. **106**, 132502 (2011).
94. W. Satuła, J. Dobaczewski, M. Konieczka, W. Nazarewicz, arXiv:1307.1550 (2013).
95. PREX-II Proposal to Jefferson Lab, `http://hallaweb.jlab.org/parity/prex/prexII.pdf`.
96. CREX Proposal to Jefferson Lab, `http://hallaweb.jlab.org/parity/prex/c-rex2013_v7.pdf`.
97. A. Tamii, Acta Phys. Pol. B **44**, 571 (2013).
98. S.K. Bogner, R.J. Furnstahl, H. Hergert, M. Kortelainen, P. Maris, M. Stoitsov, J.P. Vary, Phys. Rev. C **84**, 044306 (2011).
99. P. Maris, J.P. Vary, S. Gandolfi, J. Carlson, S.C. Pieper, Phys. Rev. C **87**, 054318 (2013).
100. M. Stoitsov, M. Kortelainen, S.K. Bogner, T. Duguet, R.J. Furnstahl, B. Gebremariam, N. Schunck, Phys. Rev. C **82**, 054307 (2010).
101. Nuclear Computational Low-Energy Initiative, `http://computingnuclei.org`